Numerical simulation of orographic rainbands

Sandrine Anquetin, Fabien Miniscloux, Jean Dominique Creutin, Stephanie Cosma

Numerical simulation of orographic rainbands

Sandrine Anquetin, Fabien Minsicloux, and Jean-Dominique Creutin

Laboratoire d'étude des Transferts en Hydrologie et Environnement, UMR 5564 CNRS, UJF, INPG, IRD, Observatoire des Sciences de l'Univers de Grenoble, Grenoble, France

Stéphanie Cosma

Laboratoire d'Aérologie, UMR 5560 CNRS, UPS, Observatoire Midi-Pyrénées, Toulouse, France

Received 26 February 2002; revised 23 August 2002; accepted 15 January 2003; published 12 April 2003.

[1] This study, based on a statistical analysis of simulated warm rain event and radar data, aims at highlighting the main physical mechanisms that lead to organize shallow convection on the relief. The region of investigation, the Cévennes-Vivarais, is located in the southeast part of France. Radar images from the Cévennes experiment (fall 1986–1988) reveal a characteristic and repetitive structure of the rain distribution organized in narrow bands or plumes, oriented south-north in the case of stationary southerly Mediterranean flow. The event of 14 November 1986 has been selected and constitutes the data set of this numerical study. This work is closely associated with the previous work by *Miniscloux et al.* [2001] which presents in detail the results of a geostatistical analysis of the radar data set extracted from the Cévennes experiment data base. The main results highlight the physical characteristics and the dynamics of the rain patterns. Following the recent work of *Cosma et al.* [2002], high-resolution (Δ = 1 km) simulations have been continued with the nonhydrostatic three-dimensional (3D) atmospheric model MesoNH, in order to reproduce the observed rainbands over the Cévennes region. The numerical model correctly reproduces the structure and the dynamics of the rainbands. The geostatistical analysis has been applied for the simulated rain fields. The model slightly overestimates the northward advection velocity of the rain cells within the bands (75 km h^{-1} against 60 km h^{-1} for the observation), and the simulated rainbands are narrower and more organized around the N180° direction than the observed rain field. The comparison allows the qualification and validation of the choice of the numerical methodology and realism of the physical parameterizations. The analysis of the 3D simulated fields confirms the physical mechanisms responsible for the rain organization demonstrated by *Cosma et al.* [2002] through idealized simulations. The statistical analysis highlights the presence of mean topographic features under low-level convergence zones composed of a succession of ridges and penetrating valleys orientated east-west. The rainbands are generated upstream of these topographic features and enhanced on the leeside due to the convergence created by the flow deflection around the obstacle and its penetration into the valleys. The simulated triggering takes place further to the south than the observed one, and the triggering is active as soon as the relief is suitably described in the model. *INDEX TERMS:* 1854 Hydrology: Precipitation (3354); 3322 Meteorology and Atmospheric Dynamics: Land/atmosphere interactions; 3329 Meteorology and Atmospheric Dynamics: Mesoscale meteorology; 3210 Mathematical Geophysics: Modeling; *KEYWORDS:* nonhydrostatic modelization, orographic rains, geostatistical analysis, radar

Citation: Anquetin, S., F. Minsicloux, J.-D. Creutin, and S. Cosma, Numerical simulation of orographic rainbands, *J. Geophys. Res.*, *108*(D8), 8386, doi:10.1029/2002JD001593, 2003.

1. Introduction

[2] Understanding the physical processes that lead to orographic precipitation has its importance in domains such as weather and climate prediction or water management. Mountainous areas affect atmospheric circulation over a wide range of scales, contributing to an uneven repartition of moisture and rain in space and time. Understanding the link between temporal and spatial variations of rainfall distribution over complex terrain is therefore a great challenge. The runoff production of mountainous watersheds will be very sensitive to this distribution.

[3] At synoptic scale, the orographic influence has already been well documented and analyzed. The forced lifting of air masses by mountain ranges is known to trigger

0148-0227/03/2002JD001593

Meso-scale Convective Systems (MCS) in summer conditions [*Cotton and Anthes*, 1989] and to modify extra tropical cyclones under winter conditions [*Browning*, 1980; *Lin*, 1993]. At mesoscale, the difficulty in studying orographic rain structure partly stems from the limitations of rain gauge networks. The density of rain gauge network typically decreases with altitude. In the French Alps, for example, there are no more recording rain gauge stations above 1800 m [*Kieffer-Weisse and Bois*, 2001]. Moreover, the measurement quality is sensitive to local conditions in mountainous areas [*Sevruk and Klemm*, 1989]. Therefore radar offers an interesting opportunity to explore and to analyze orographic control of precipitation fields [*Tateya et al.*, 1991; *Fujiyoshi et al.*, 1996; *Warner et al.*, 2000; *Miniscloux et al.*, 2001; Y. Suzuki et al., Study of the dependence properties of rainfall distributions on topographic elevation, submitted to *Journal of Hydroscience and HydraulicEngineering*, 2002]. Even if rainfall detection by radar is significantly influenced by the topography itself [*Joss and Waldvogel*, 1990], the radar observation can not be ignored in characterizing the orographic rain structure and its associated time and length scales [*Nakakita et al.*, 2001]. Numerical modeling is a natural and complementary tool for the understanding of orographic precipitation. *Barros and Lettenmaier* [1994] propose a review of the different numerical approaches and their associated restrictions and limitations. The 3D modeling of both circulation dynamics and cloud microphysics over a wide range of space and timescales leads to the conflict between resolution requirements and computer resources. Recent works [*Kuligowski and Barros*, 1999; *Reinking et al.*, 2000; *Ducrocq et al.*, 2000; *Cosma et al.*, 2002] show that meteorological models are now able to reproduce the atmospheric dynamics and to provide realistic rainfall distributions at mesoscale.

[4] The most investigated orographic processes are reviewed by *Smith* [1979] and *Barros and Lettenmaier* [1994]. *Lin* [1993] reviewed several prominent weather problems related to orographic effects on the circulation and the track of a typhoon that impinges on Taiwan. Both windward and leeward orographic effects are important [*Barros and Kuligowsky*, 1998]. Local thermal gradients can initiate convective currents. It is known that the low-level clouds produced by orographic lifting and low-level vortex feed precipitation formed at higher altitudes [*Bergeron*, 1965; *Fujiyoshi et al.*, 1996].

[5] This work is closely associated with a recent paper which analyzes orographic rainbands observed with a weather radar in a Mediterranean mountain range of Southern France [*Miniscloux et al.*, 2001] (later referred to as MCA). Under stable southerly flow conditions associated with the warm sector of a perturbation, narrow and south-north orientated rainbands develop over the relief zone and remain stationary for hours. Rain intensities are therefore more sustained over the hills than over the foothills. Triggered by relief shoulders separating southeast facing valleys, the rainbands are regularly spaced by typically 15 km. They contain northward moving rain cells traveling at a velocity slightly lower than the wind measured at a high elevation weather station (Mont Aigoual: 1565 m, referred to as Aig on Figure 1). These rain cells have a periodicity of roughly 40 minutes. *Cosma et al.* [2002] use the research nonhydrostatic model MesoNH [*Lafore et al.*, 1998] to successfully simulate such a warm precipitation event organized in rainbands. They show that as long as the numerical resolution is high enough (Δ = 1 km), the model can reproduce the rain structure in terms of rain accumulation as well as positioning with respect to topography.

[6] Such static rain patterns, produced by shallow orographic convection, have a typical scale directly related to the typical scale of the topographic features. *Tateya et al.* [1991] showed that a rainband is formed by the presence of the wall like mountain range in Hokkaido Island. Their simulations concluded that scales less than 5 km have no significant effects on the topographic rainfall pattern.

[7] The orographic rain pattern produces less intense rain intensities, as they result from shallow instead of deep convection (typically less than 10 versus several tens of mm h^{-1}). Nevertheless, their hydrological impact is critical, due to the strong spatial heterogeneity and the significant amounts of rain accumulated over time [*Barros and Kuligowski*, 1998].

[8] Focusing on this meteorological phenomenon, this paper aims to answer questions related to the following issues: (1) persistence in space of the rainbands, (2) localization of rain cells with respect to the relief, (3) dynamics of the rain cells and (4) origin of the triggering effects and its associated physical mechanisms.

[9] We use the reliable weather database from the Cévennes 1986–88 hydrometeorological experiment to qualify numerical results. The simulated meteorological fields help the understanding of the 3D physical mechanisms responsible for the rainband structure. Moreover, the comparison between the observed and simulated rain fields illustrates the statistical properties of the orographic rain field in a mountainous area. Through this detailed analysis, we discuss the limitation of the model.

[10] The meteorological model and the data set used in this study are presented in Section 2. Model results and the comparative statistical analysis of observed and numerical rain fields are discussed in Sections 3 and 4. Section 5 offers conclusions and perspectives.

2. Meteorological Data Set and Model Used

2.1. Description of the Available Data Set

[11] The data set used in this study, is taken from the Cévennes experiment, which took place in the southeast of France (Figure 1) during three consecutive falls from 1986 to 1988. The Cévennes region altitude ranges from sea level up to 1500 m in roughly 30 km. According to elevation contours, three sectors have been identified: (1) a flat sector around the city of Nîmes (below 200 m), (2) a hilly sector (between 200 and 500 m) and (3) a mountainous sector (above 500 m). The thick solid lines on Figure 1 characterize these three sectors.

[12] This region experiences prolonged rain events capable of producing catastrophic floods over a wide range of river basin sizes (from 100 up to 10,000 km^2). Therefore, one of the principal goals of this field experiment was to evaluate the usefulness of radar rainfall monitoring in mountainous areas for hydrological purposes.

[13] The S-band dual polarized radar ANATOL and an operational meteorological network of 42 rain gauges, were operated over a study area covering roughly 5000 km^2 (see Figure 1). The mobile radar was located at an altitude of

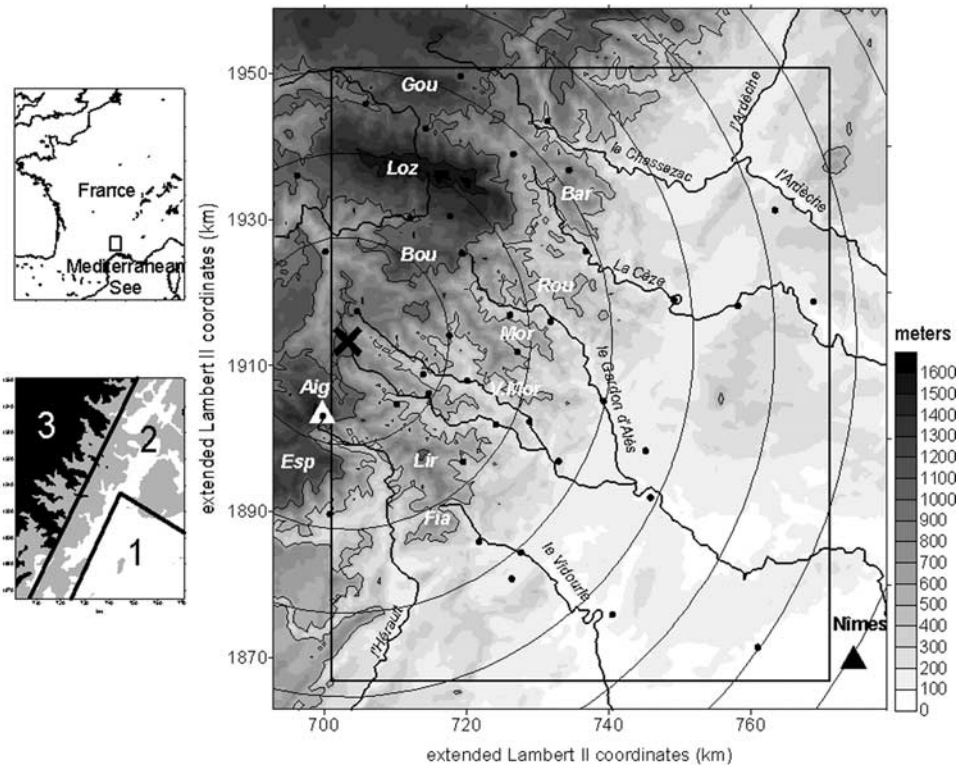

Figure 1. Relief of the studied area. The DTM resolution is 75 m (Aig, Mont Aigoual (1565 m); Bar, Serre de Barre; Bou, Montagne du Bougès; Fia, Montagne de la Fiage; Gou, Montagne du Goulet; Lir, Montagne du Liron (922 m); Loz, Mont Lozère; Mor, Montagne de Mortissou; Rou, Montagne du Rouvergue (695 m); V.Mor, Montagne de la Vieille Morte (920 m); the radar site (crosses); the weather stations of Mont Aigoual and Nmes (triangles) and 42 rain gauge stations (circles). On the left side: the general location in Europe (top box) and the 3 topographic sectors (bottom box).

1030 m near the village of Barre des Cévennes. Almost 150 hours of data were recorded with a frequency of 8 minutes. After radar processing (for more details, see *Andrieu et al.* [1997]), the images are available at a spatial resolution of 1 km. These images show more than 1000-mm of rain accumulated in some locations. They corresponded with four well-organized cyclonic perturbations. Prolonged and widespread rain events were associated with these perturbations.

[14] The data set used in this paper is associated with one of these perturbations and is composed of 128 instantaneous radar pictures that represent 16 consecutive hours on 14 November 1986. The selected hours correspond to the two main criteria: (1) the rain patterns are to be confined to the relief and to remain steady at the scale of the observed area, (2) associated to this rain pattern, the atmospheric flux is to be almost saturated with humidity and the wind must blow for several hours from an almost constant direction (N180°E). The mean vertical profile of reflectivity showed that for the selected period, the highest radar echoes are roughly 1.5–2 km above the mountain tops which are 1.5 km high [*Miniscloux et al.*, 2001]. No bright band effect is present.

2.2. Description of the Meteorological Model Used

[15] The simulations were carried out with the 3D non-hydrostatic model MesoNH, developed jointly by Météo-France (CNRM) and the Laboratoire d'Aérologie [*Lafore et al.*, 1998]. The anelastic system of equations is integrated in the system of curvilinear coordinates with nonuniform grids: geographic conformal projections on the horizontal plans and *Gal-Chen and Sommerville*'s [1975] vertical coordinates. The spatial discretization uses the C-grid formulation. Therefore, the vertical coordinate follows the relief. The temporal scheme is a three time level leapfrog with the time filter of *Asselin* [1972]. Horizontal diffusion is introduced by a fourth operator in all prognostic equations to damp the short numerical waves. Lateral boundaries have open boundary conditions. The top boundary is a rigid horizontal lid with an absorbing layer, to avoid the reflection of gravity waves.

[16] The model relies on physical packages to reproduce the different atmospheric processes such as turbulence, convection, radiative transfer, microphysical parameterizations and soil-atmosphere exchanges. The parameterizations used in the simulations are presented in Table 1. More details on the complete set of parameterizations available in the MesoNH model can be found in the scientific documentation [*Bougeault and Mascart*, 2001]. To simulate the warm precipitation event, the standard Kessler scheme is used to characterize the microphysical processes and the rain production.

2.3. Description of the Simulation

[17] The simulation was performed over nine hours, using the grid nesting technique in its one-way formulation. Four models ran together, in order to exchange information from the 50-km horizontal resolution model up to the 1-km horizontal resolution model. The nested domains are pre-

Table 1. Physical Parameterizations Used for S1

Physical Mechanisms	Horizontal Grid Size			
	50 km	10 km	2 km	1 km
Soil-atmosphere exchange model: ISBA soil model [*Noilhan and Planton*, 1989]	X	X	X	X
Turbulent scheme, k-L [*Bougeault and Lacarrère*, 1989]	X	X	X	X
Convection scheme [*Kain and Fristch*, 1993]	X	X		
Explicit microphysical scheme with no ice phase [*Kessler*, 1969]	X	X	X	X
Radiative transfer scheme, effect of the solar and infrared radiations [*Morcrette*, 1989]	X	X	X	X
Resolution nx.ny.nz	100.100.45	125.125.45		80.90.45
Vertical resolution (m)	60 m (ground) → 1000 m (top)			
Time step (s)	60	12	6	3

sented in Figure 2. Due to the lack of available information for the detailed initialization procedure [*Ducrocq et al.*, 2000], the numerical strategy summarized below was used.

[18] The simulation started at 0000 UTC 14 November 1986. The first six hours were dedicated to the initialization of the largest domain. Therefore, the larger domain (Δ = 50 km) was run alone and forced with boundary conditions given by a linear temporal interpolation of the ECMWF analyses given at 0000 UTC and 0600 UTC. Then, the domain at Δ = 10 km grid resolution was included in the simulation, and the two nested models were run for 3 hours. Finally, the four nested models were run for another nine hours. The largest domain was forced with boundary conditions given by a linear temporal interpolation of the ECMWF analyses given at 1200 and 1800 UTC. The accumulated precipitating rain in the smaller domain, with

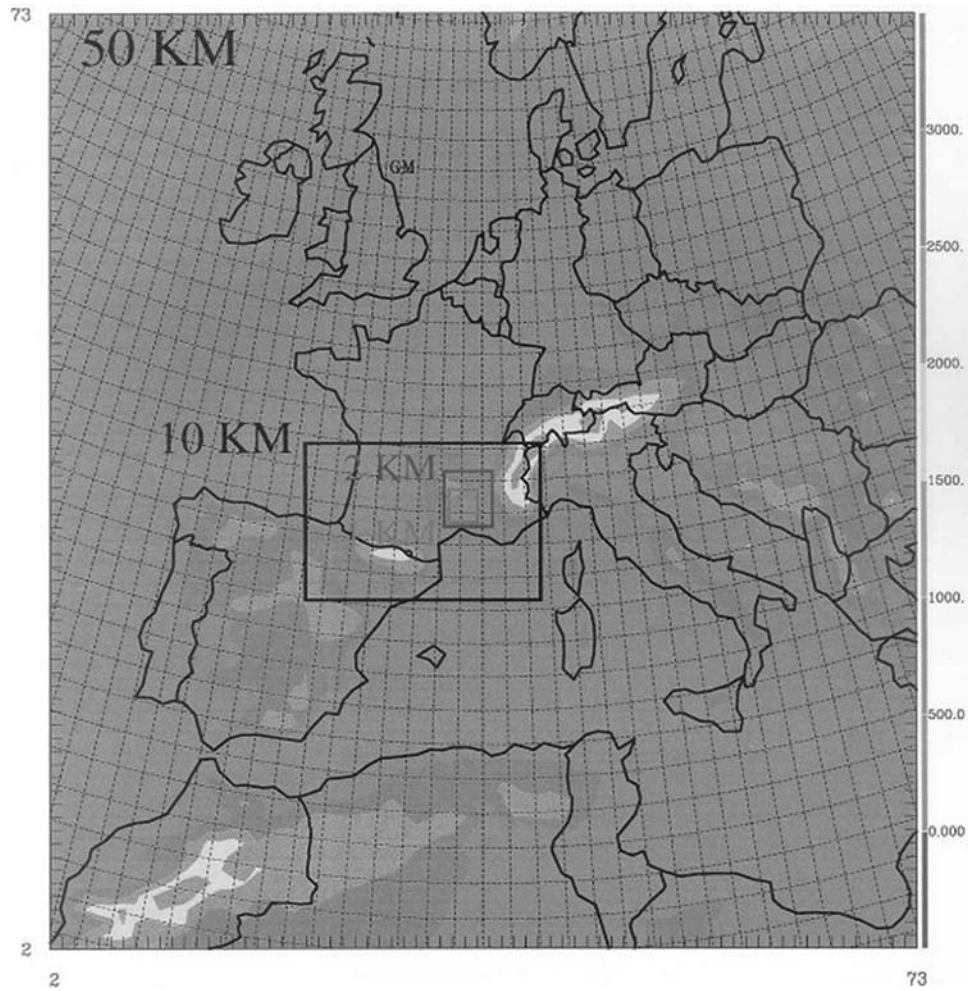

Figure 2. The four domains used for the nested simulation. The background is the 50 km orography represented with 500 m spaced isocontours.

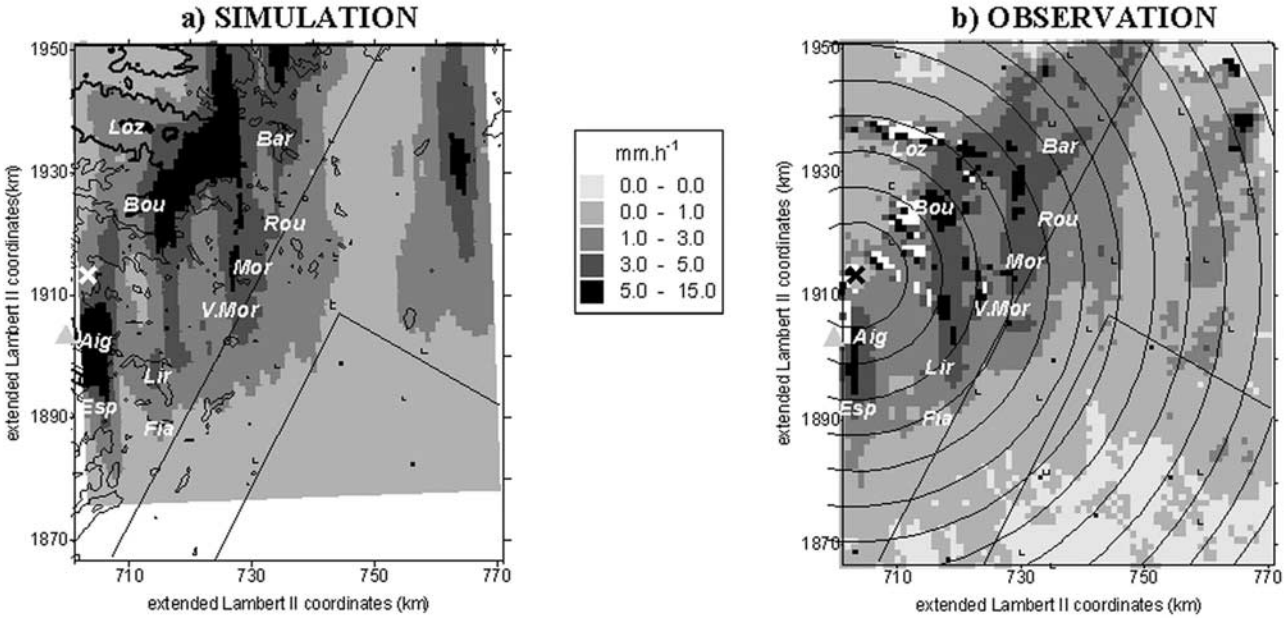

Figure 3. (a) Mean simulated rainfall rate from 900 to 1800 UTC. (b) Mean observed rainfall rate from 0500 to 2100 UTC. White pixels denote missing data.

a grid size of Δ = 1 km, was recorded every 10 min and later compared to the observed rain field.

3. Structure and Positioning of Rainbands

[19] The simulated rain fields are analyzed through the geostatistical analysis developed by *Miniscloux et al.* [2001]. The main results are discussed below.

3.1. Mean and Variance Fields

[20] The mean and the variance maps of rain intensity are presented in Figures 3 and 4. They are compared to the observed values. These maps reveal the capability of the model to reproduce the rainbands in terms of rain accumulation and its associated variability, as well as positioning with respect to topography.

[21] The global structure of the rain field is well reproduced. The precipitation pattern is confined to the hilly and mountainous sectors consisting of several N-S oriented bands. The three bands of the mountainous sector (x = 705, 718 and 730 km) are well simulated, even if the simulated field probably lacks of variability (smoother mean field and lower variance field). The two bands of the hilly sector (x = 745 and 760 km) are not as well reproduced. The band at x =

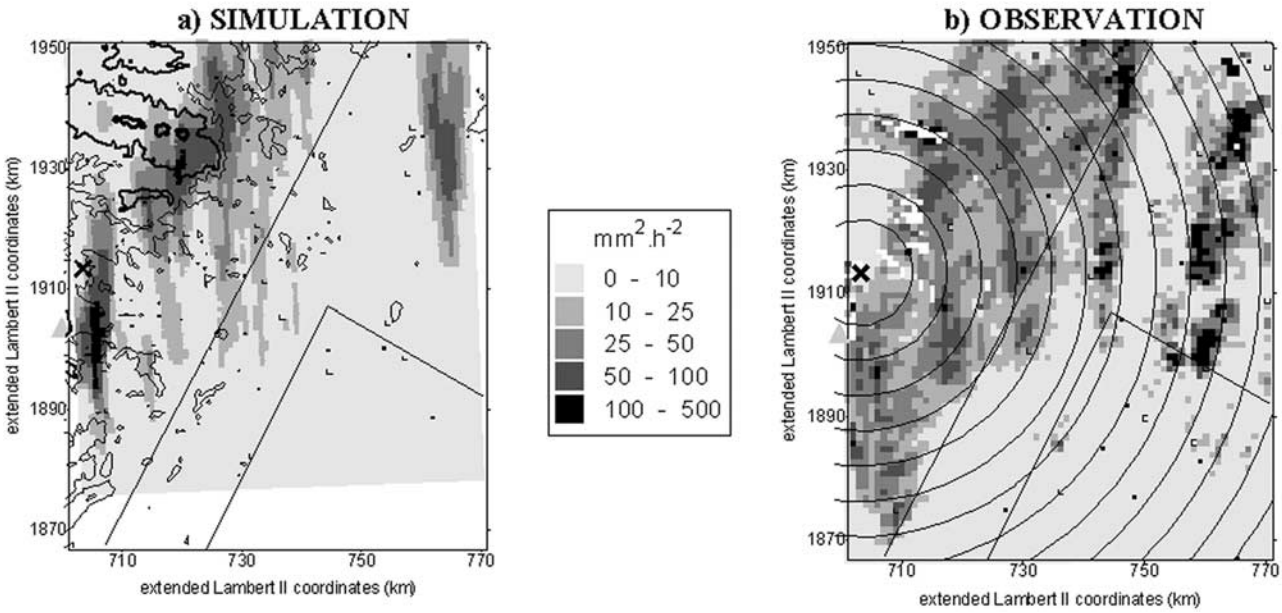

Figure 4. (a) Simulated variance of the rainfall rate from 900 to 1800 UTC. (b) Observed variance of the rainfall rate from 500 to 2100 UTC. White pixels denote missing data.

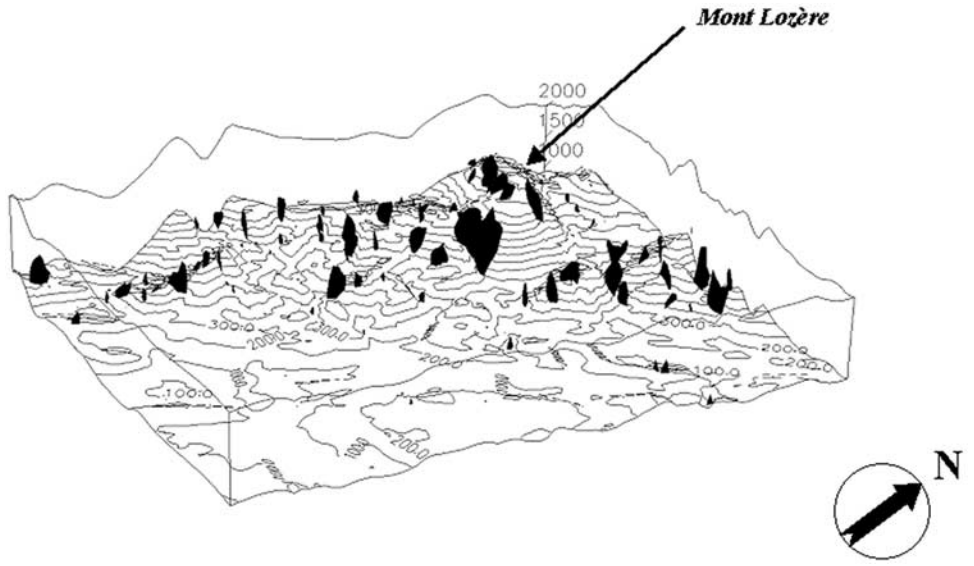

Figure 5. Vertical extension of the convergence zones for the given threshold $div\vec{U} = -0.003\ s^{-1}$.

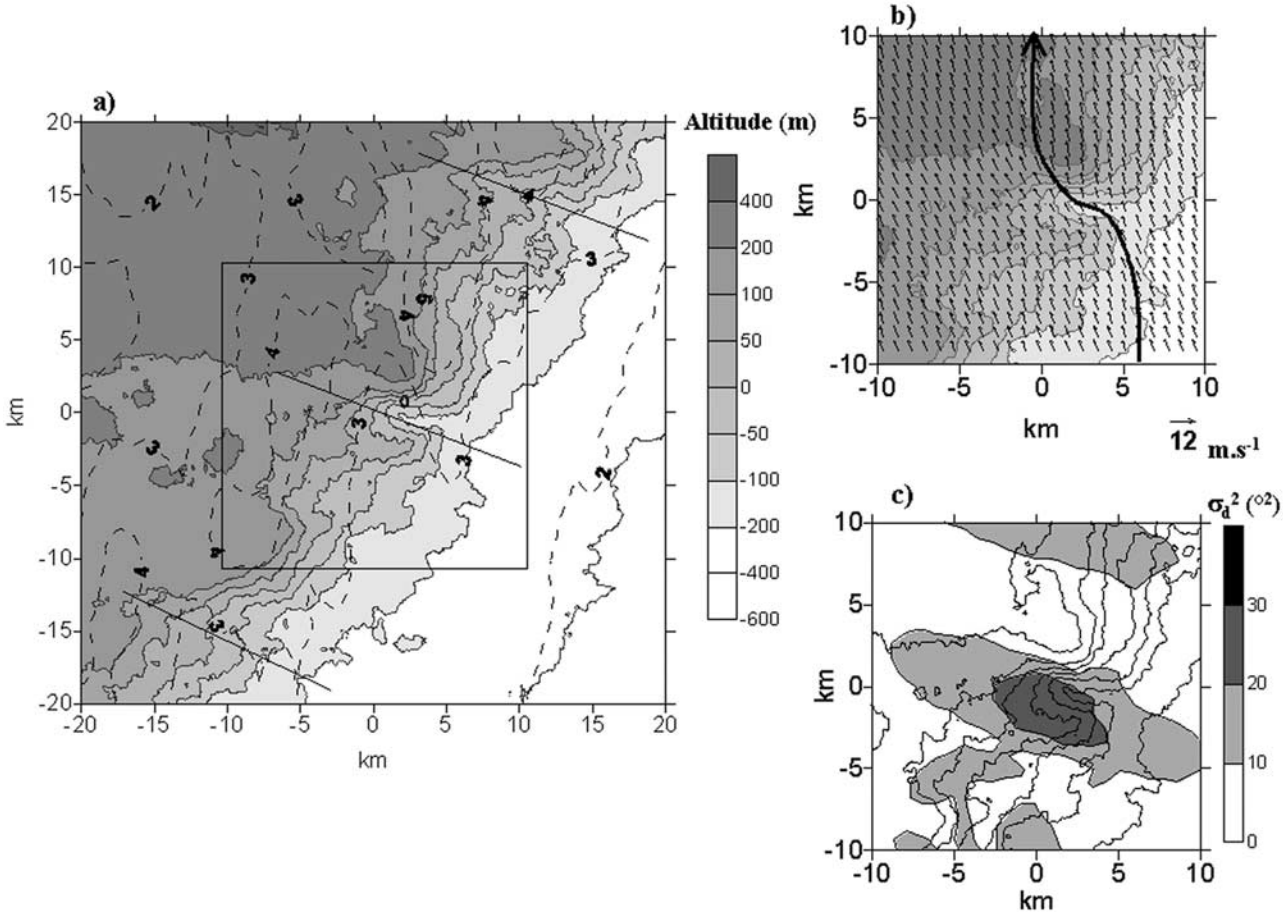

Figure 6. (a) Mean statistical rain field (dashed lines: mm) and corresponding mean underlying topography (gray scale) centered on the gravity centers of identified convergence zones. (b) Mean statistical horizontal wind above the ground (30 m). (c) Variance of the wind velocity centered on the gravity centers of identified convergence zones.

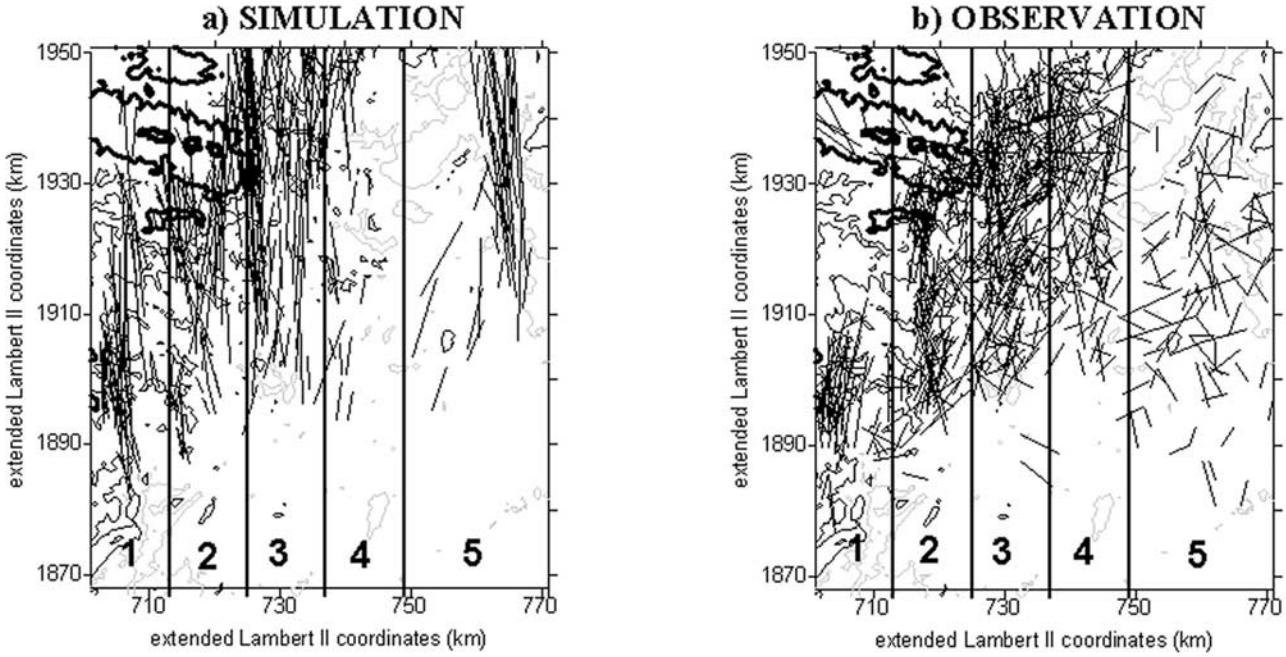

Figure 7. Major axis representation obtained with (a) the simulated rain pattern and (b) the observation data. The rain intensity threshold is 10 mm h^{-1}, and the topography is represented with the 200, 500, 1000 and 1500 m isocontours.

745 km is skipped Westward to the mountainous sector, while the band at x = 760 km is overestimated in mean and variance. In these both regions, the more distant from the radar (solid cross, Figure 1), the more important is the number of missing values as shown by *Miniscloux et al.* [2001]. This is due to ground clutter, beam blockage, the vertical profile of reflectivity effect and some residual echoes. Therefore, it is difficult to comment on the discrepancy between observed and simulated rain patterns in these regions.

[22] The simulated rain accumulation is slightly overpredicted compared with the observed rain field. The presence of a high altitude obstacle like Mont Lozère (x = 715 km, y = 1940 km, z = 1500 m) has a strong influence on the flow field and therefore, on the main rain production processes. The flow is blocked, and due to the large width of the mount, an upward motion is produced, leading to the intense rain precipitation zone between corridors two and three. The observations do not present the same rain pattern around this mount, where most of the missing values (shown with white pixels) are due to ground detection.

[23] On the basis of idealized numerical simulations, *Cosma et al.* [2002] show that this type of rain organization in bands results from the combination of several mechanisms involving flow dynamics above and around small scale topographical disturbances such as orographic lifting, vertically propagating mountain waves and lee side convergence.

[24] To investigate further the role of small-scale topographical disturbances on the resulting rain field, a Lagrangian approach was used to analyze the simulated 3D-flow field of 14 November. As flow convergence is suspected to be the origin of the rain formation, the first step is dedicated to the identification of the convergence zones. The horizontal divergence flux is computed in the whole domain on each model level. Then, the convergence zones are identified for different negative thresholds of the divergence field. It is found that a smaller threshold (around 0 s^{-1}) leads to convergence zones that have a larger vertical extension. As we are interested in the dynamics of the lower layers of the atmosphere, a -0.003 s^{-1} threshold is found to be a good compromise between the number of convergence zones and their vertical extension. Furthermore, this threshold corresponds to the mean value of the convergence field. To illustrate our purpose, the convergence zones, calculated with the mean velocity field, are plotted in Figure 5.

[25] Then, the issue lies within the computation of the mean underlying topography around the gravity center of the convergence zones, in order to determine whether there is a prevailing type of topography below these convergence zones. The gravity centers are referenced with their coordinates (x_b, y_b) expressed in the whole domain D. The mean underlying topography $\overline{H_b}$ is extracted from the digital terrain model (DTM: terrain elevation described at a resolution of 75 m in the horizontal and 1 m in the vertical) by using a moving window, centered on the N_c gravity centers of the convergence zones. It is expressed by:

$$\overline{H_b}(X,Y) = \frac{1}{N_c} \sum_{(x_b,y_b)\in D} \left(H(x_b+X, y_b+Y) - H(x_b,y_b)\right) \quad (1)$$

where (X, Y) are the window coordinates and $H(x, y)$ is the terrain elevation.

[26] The underlying topography is mapped in Figure 6a. The main slope orientated southeast-northwest is clearly identified in Figure 6a. This is a characteristic of the

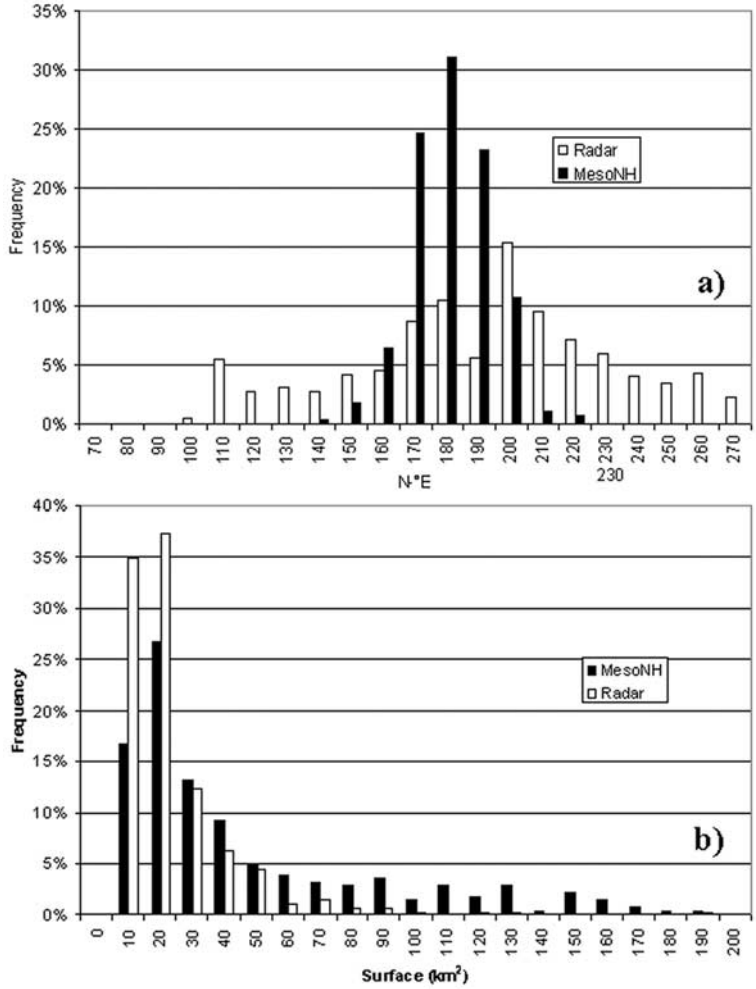

Figure 8. (a) Statistical distribution of the major axis orientation (in N°E) of the rain cells. (b) Statistical distribution of the surface of the rain cells. The rain threshold is 10 mm h^{-1}.

Cévennes-Vivarais region. The penetrating valleys orientated east to west appear without ambiguity on the east side of the gravity center of the convergence zones (0, 0). This confirms the major role of the small-scale topographical characteristics on the dynamics of the lower layers of the atmosphere. Penetrating valleys are less readable but still apparent in the southwest and northeast, they are noted with an inclined line. The spacing between penetrating valleys is around 15 km, another characteristic of this region.

[27] The mean rain field $\overline{R_b}$ centered on the gravity center of the convergence zones is represented in Figure 6a with the dashed black lines and is expressed by:

$$\overline{R_b}(X,Y) = \frac{1}{N_c} \sum_{(x_b,y_b)\in D} R(x_b + X, y_b + Y) \qquad (2)$$

Through this synthetic representation of the dynamics and the resulting rain field, it appears that the maximum of precipitation is located on the lee side of the gravity centers with a slight deflection to the east according to the general orientation of the topography. Again, on Figure 6 rainbands (4 mm) appear with a spacing of 10–15 km and are located on the lee side of penetrating valleys.

[28] In Figure 6b, the mean horizontal wind field at the first grid point (30 m above the ground) centered on the gravity centers is represented on a smaller domain presented in Figure 6a. Its coordinates are expressed by:

$$\overline{u_{b,i}}(X,Y) = \frac{1}{N_c} \sum_{(x_b,y_b)\in D} u_i(x_b + X, y_b + Y) \;\; u_i = U \text{ or } V \qquad (3)$$

[29] The superimposition of these two maps gives a synthetic view of the dynamics of the horizontal wind field associated with the topography below the convergence zones. One can note the channeling in the penetrating valleys. To give an idea of the variability of the mean velocity field around the gravity centers of the convergence zone, the variance of the wind direction at the first model level (30 m above the ground) is plotted in Figure 6c. The variability is more important upwind of the penetrating valleys. Nevertheless, it is confined to 5° around its mean direction plotted in Figure 6b and therefore confirms the static behavior of the rain organization.

[30] Through these observations based on a synthetic representation of the dynamics and resulting rain field, the following interpretations are proposed: (1) the N120°E orientated valleys channel the flow and uplift air masses

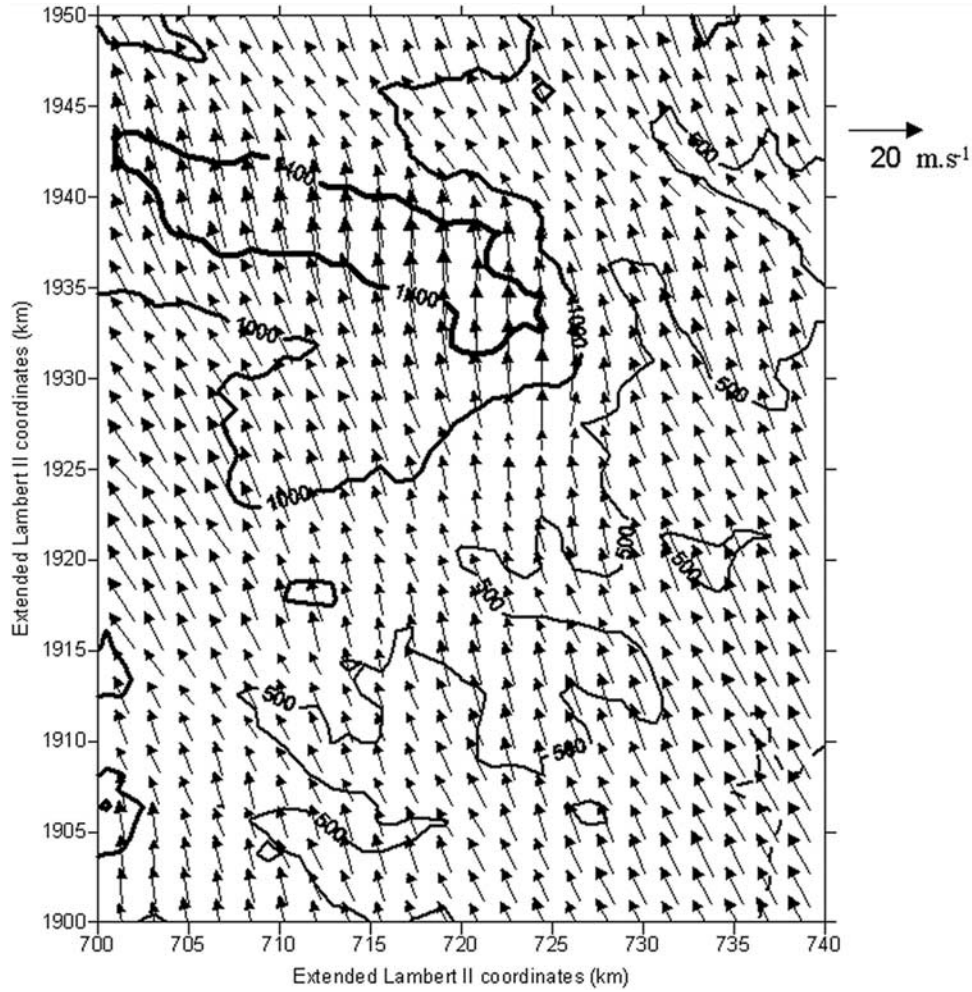

Figure 9. Horizontal cross section (at 30 m above the ground) of the mean simulated horizontal wind at the surface.

and (2) the upward motion of the air masses in the deep valleys creates convection, which produces rain on the leeward of the obstacle.

3.2. Rain Cells and Triggering Areas

[31] MCA describes the rain pattern by a distribution of rain cells, characterized by a closed contour (defined by a major axis and a surface) where the rain intensity exceeds a given threshold. It is shown that a 10 mm h^{-1} threshold is a good compromise between the size and the number of rain cells; the main conclusions do not significantly depend on this threshold.

[32] The major axis is plotted for each identified rain cell, for the simulated rain field and the observed data in Figure 7. The distribution of direction of the major axis and of the surface of the rain cells are displayed in Figure 8. These figures suggest the following comments:

[33] The simulated rain pattern is more organized around the N180°E direction than the observed rain field in Figure 8a. As discussed in MCA, the presence of Mont Lozère disturbs radar detection and obstructs the cell detection. The rain cell can not be found to pass over the mountain. They are ''forced'' to have an inclined direction along the N260°E orientation of Mont Lozère and the submode N260°E appears in the radar data set, whereas the simulated orientations are focused around its mean value N180°E.

[34] The distribution of axis orientation is globally symmetric for the two sets of data. The mean value is different: N180°E for the simulation and N200°E for the observed data. The two submodes are also different: N170°E and N190°E for the simulation; N180°E and N210°E for the observed data. MCA argue that the two submodes are respectively associated to the cells contributing to the bands and the cells moving between the bands. Moreover, the N210°E direction characterizes the mean slope orientation, which has an impact on rain cell orientation. The simulation lead to a different analysis. The flow field is confined around the major flux direction (N180°E) and its vertical amplitude is sufficient to allow the flow to pass over the relief crest of Mont without any contribution along the N210°E direction. There is no tangential component of the flow field along the relief shoulder. The mean horizontal flow field at 30 m above the ground is plotted above the topography in Figure 9. The southerly direction is dominant and no significant tangent component is present. Therefore, one possible

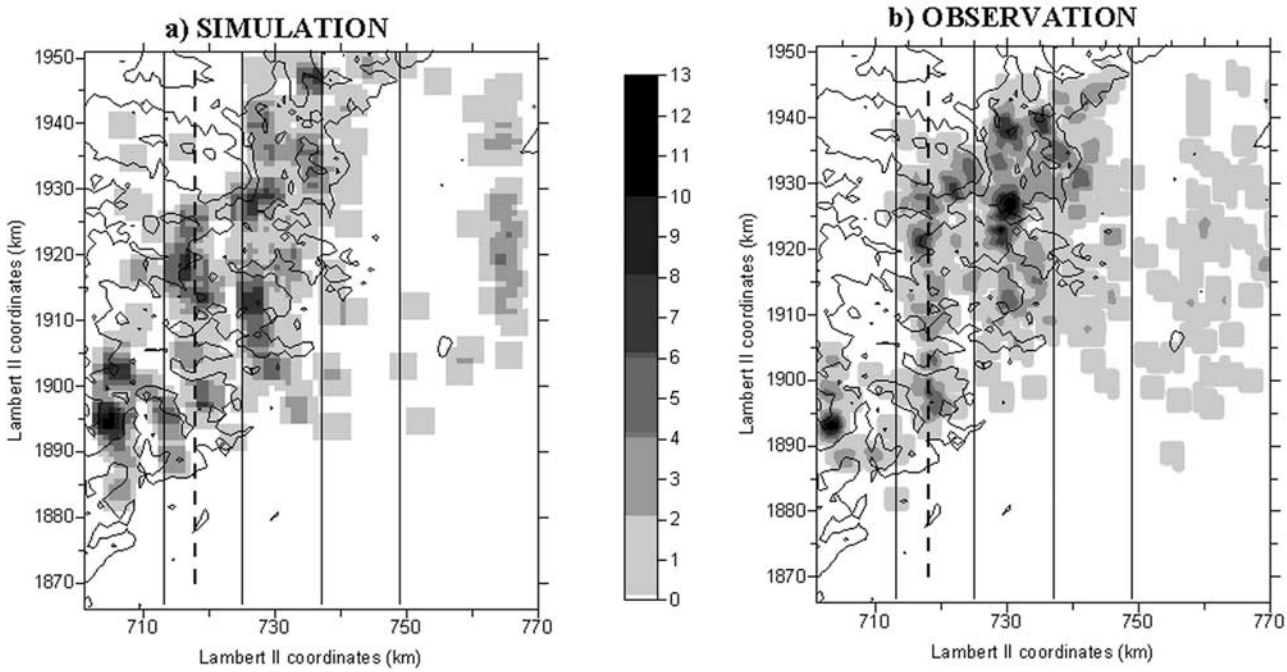

Figure 10. Number of triggering points, from 0900 to 1800 UTC, in a moving 4×4 km^2 windows for a threshold $\tau = 10$ mm h^{-1}. (a) Simulation. (b) Observations. The relief contour line corresponds to 500 m high. The dashed line indicates the 2^d rainy axe (X = 718 km) where the RTI is performed.

interpretation is that the simulation does not reproduce the small-scale instability that determines the variability of the rain cell orientation.

[35] The surface of the simulated rain cells in Figure 8b is found to be larger than for the observations. This leads to the overestimation of the simulated rain intensity (Figure 3). This has already been mentioned by *Pinty et al.* [2001] and is attributed to the choice of the physical parameterizations, in particular the microphysical scheme. The Kessler formulation of the warm microphysics has been shown to have a poor cloud autoconversion efficiency which does not reproduce the detailed dynamics of the cloud and precipitation processes [*Pinty et al.*, 2001]. This scheme parameterizes the humidity in the cloud to increase to a given threshold; then, the precipitation processes occur as a reservoir emptying.

[36] The rain cell distribution analysis is complemented with the map of triggering point densities over the studied domain, presented in Figure 10, and from 0900 UTC to 1800 UTC. Triggering points are defined as the southern end of the major axis of the rain cell. Their number is computed in a moving window of 4×4 km^2 centered on each 1×1 km^2 pixel. The five bands are naturally present. The model correctly reproduces the main characteristics of the triggering processes. The maximum of triggering point is found to be the same by the model and the observation.

[37] Figure 10 also highlights the prevailing zones of triggering and especially the different relief features that influence rain production. The comparison between the results of the simulation and the observation shows that some relief shoulders are clearly identified both by the observation and the simulation. The simulated triggering is slightly more active in the southern part of the relief. As observed through the analysis of the radar data, the rain triggering occurs on the southern part of Mont Lozère and the lee side of the mount does not present any rain cell triggering.

[38] This map also confirms the main mechanism responsible for rain production suggested by the model. Above flat terrain, the model does not produce any rain cells whereas the observations show a few rain cells in this region. Nevertheless, rain production is active even above very small hills (e.g., x = 760 km Lambert II coordinate) as soon as the relief is well described by the model.

4. Cell Dynamics Inside the Rainbands

[39] A "range time indicator" technique is applied (later referred to as RTI) to analyze the space and time fluctuation of the rain inside the bands. The results for the second corridor (one of the two more active rainbands in the mountain region, indicated with the dashed line on Figure 10) will only be discussed here. A section parallel to the prevailing wind direction is extracted for each simulated or observed rain field at the coordinate x = 718 km, which corresponds to the selected rainband. The extraction frequencies are slightly different for the model and the observation and are respectively 10 min and 8 min. For practical reasons, the rain field is averaged within a band of three pixels ($x \pm 1$ km).

[40] Figure 11 displays the comparison between the RTI obtained from the simulated rain field and the one obtained from the observed data. The shape of the underlying topographic profiles and the associated triggering points are also displayed.

[41] These maps reveal the presence of moving rain cells both for the observation and the simulation. An inclined pattern describes the propagation of a rain cell in space.

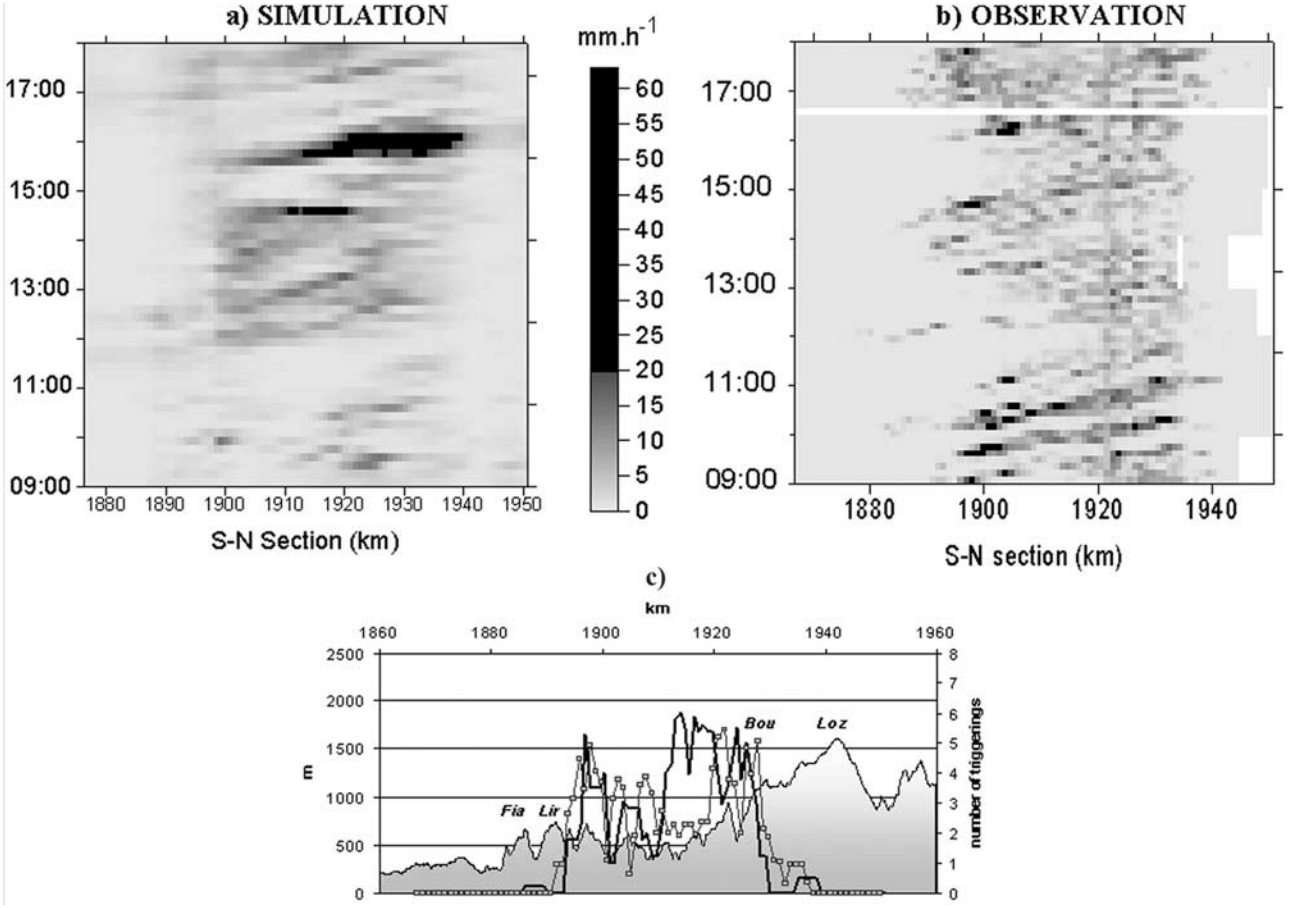

Figure 11. Range time indicator (RTI) corresponding to the rainbands in the second rainy band at X = 718 km. (a) Simulation, (b) Observed values. The related topographic profile is represented in Figure 11c with the number of triggering along the section (thick solid line for the simulated number of triggering and dashed line for the observed number of triggering).

These inclined patterns appear both for the simulation and the observation, but are smoother for the simulated rain field.

[42] The origin of the different inclined patterns coincides well with the identified triggering points. The simulated triggering is very well reproduced, and as observed in Figure 10, the second peak of triggering (at y = 1913 km) is located approximately 10 km upwind of the observed peak (y = 1920 km). This result is difficult to explain, although the parameterization of the autoconversion dynamics is probably responsible for this behavior. Nevertheless, the two peaks have the same intensity.

[43] The slope of the inclined pattern corresponds to the propagation speed of the rain cell. The rain cells are regenerated at the frequency observed, with the periodicity in time of these patterns. The simulation correctly reproduces these dynamics. Nevertheless, this velocity is overestimated by the model (75 km h^{-1} against 60 km h^{-1} for the observed data). This discrepancy is probably due to the main orientation of the rain cell production (Figure 8a). The simulated rain production is associated with the general flux orientated N180°E that is more intense. Moreover, the difference between the real topography and that simulated at 1-km resolution may be another explanation. The simulated relief is naturally smoother, leading to a lesser degree of slowing of the atmospheric flow.

[44] RTI pictures can be analyzed with the 2D variogram function $\gamma(Y, T)$, to evaluate the periodicity of the triggering and the propagation speed of the rain cell. The 2D variogram function drawn in Figure 12 is expressed by:

$$\gamma(Y,T) = \frac{1}{2N_{Y,T}N}\sum_{i=1}^{N}\sum_{k=1}^{N_{Y,T}}\{R[(y_k,t_k),i] - R[(y_k+Y,t_k+T),i]\}^2 \quad (4)$$

where y_k characterizes the latitude and t_k the time of the rain field R of the ith picture (i.e. N = 128 for the observation and N = 54 for the simulation). Y and T are the relative coordinates of a point in a moving window of the size $[(-Y_{max}, Y_{max}), (-T_{max}, T_{max})]$, where Y_{max} = 35 km and T_{max} = 200 min.

[45] The mean quadratic gradient of rain intensities over a moving window highlights the autocorrelation of the rain production process in time and space.

[46] Along a fixed position in space, the variogram reveals the autocorrelation of rain intensities in time. The decorrelation time is slower for the simulation (around 20 min) than for the observation (less than 10 min), taking 15 mm^2 h^{-2} as a limit to 50 % of the explained variance. The regularly spaced submaximums of the variogram (17 mm^2 h^{-2})

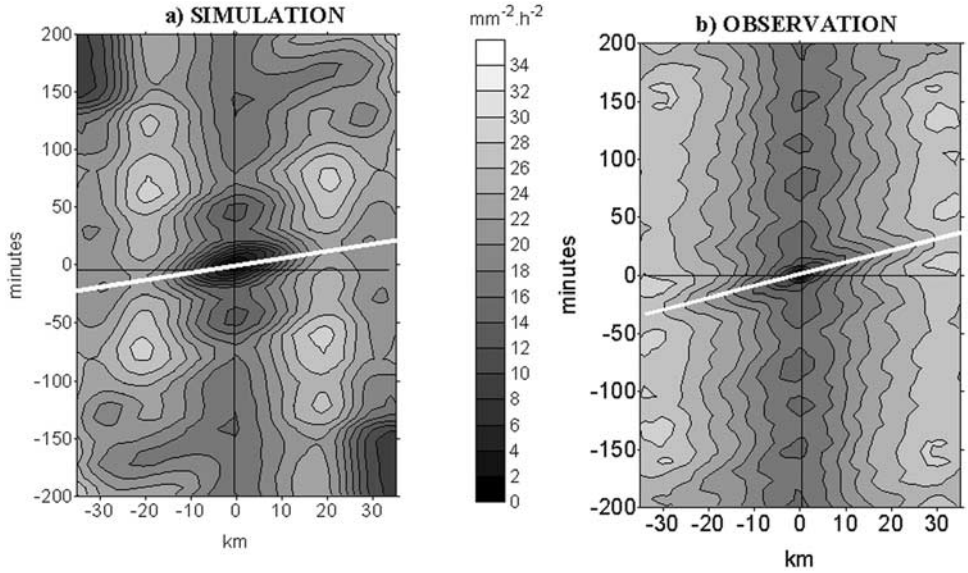

Figure 12. Two-dimensional variogram maps of RTI calculated for the second rainy band at X = 718 km. (a) Simulation. (b) Observed values. The thick solid lines give the slope of the inclined patterns and materialize the velocity of the rain cells.

revea la time periodicity of the process. For both the simulation and the observation, the time frequency is around 80 min.

[47] For a fixed time, the decorrelation length of the simulated rain field in the south-north direction is longer (approximately 10 km) than for the observed rain field (around 5–7 km), taking 15 $mm^2\ h^{-2}$ as a limit to 50 % of explained variance.

[48] The advection of the rain cells leads to a space and time coherence of the rain field and is estimated by the slope of the inclined patterns drawn in Figure 12. The obtained values are approximately the same as those previously obtained from the RTI analyses (60 km h^{-1} for the observation and 75 km h^{-1} for the model).

5. Conclusions

[49] The mesoscale model MesoNH has simulated the precipitation event that occurred on 14 November 1986 in the Cévennes region. This event was characterized by a spatial distribution of precipitation in the form of bands. These bands are orientated South North and remain concentrated along the same axis during the entire episode.

[50] This paper aims to answer some questions about this meteorological phenomenon.

[51] The observation and the 3D simulation show that for a stationary southerly Mediterranean flow, these rainbands are persistent and are more active and more stable over the mountains than over the hilly area. This is due to small-scale topographical disturbances, such as penetrating deep valleys, which create deviations in the lower atmospheric layer leading to persistent convergence zones. Upwind of these zones, the rain intensity is maximum.

[52] The localization of the rain cells is therefore strongly associated with the topography. The model can reproduce this rainband structure and the localization of the bands as long as the resolution is high enough. Nevertheless, the results of the simulation show that the rain cell orientation is confined around the general flux direction. The model does not reproduce small-scale instabilities that lead to a less orientated rain production, as observed with the radar.

[53] The RTI technique helps to identify advecting rain cells that constitute these rainbands. The comparison between the observation and the results of the simulation shows that the model does not reproduce in detail their pulsation. Their northward velocity is slightly overestimated, probably due to the prevailing rain production orientation (N180°E) and to the simulated topography that is smoother than in reality. Nevertheless, the simulated triggering is very well reproduced, but the choice of the microphysics fails, leading to larger rain cell surfaces, as previously observed by *Pinty et al.* [2001]. This later point should be investigated further, through idealized simulation, using the same domain and looking at the impact of some parameterizations (microphysical scheme, type and density of the aerosols) on the resulting precipitation.

[54] A thorough study would require a larger and more complete data set. This would allow analysis of the conditions required for the development of such orographic rain, and to investigate the interaction between the local modification of the flow (wind speed and direction, relative humidity and temperature) and the resulting precipitation. Few continuous high quality observations (radar, high density rain gauge network) are available in mountainous regions and around the Mediterranean, except the recent data set collected during the MAP (Mesoscale Alpine Programme [*Bougeault et al.*, 2001]) experiment, located in the Italian Alpine region during fall 1999. Moreover, in the Cévennes-Vivarais region and since January 2001, a Hydrometeorological Observatory has been created to build up a database for hydrological and meteorological observations. This Observatory will provide a new opportunity to further investigate the role of small-scale orographic forcing

on the precipitation distribution, and to estimate its hydrological impact in terms of runoff and discharge.

[55] **Acknowledgments.** The current study has been supported by the PATOM and PNRH research programs of the CNRS-INSU, the French Institute for the Universe Sciences. The numerical simulations were carried out on the NEC of the IDRIS (CNRS) computing center.

References

Andrieu, H., J. D. Creutin, G. Delrieu, and D. Faure, Use of a weather radar for the hydrology of a mountainous area, part I, Radar measurement and interpretation, *J. Hydrol.*, *193*, 1–25, 1997.

Asselin, R. I., Frequency filter for time integration, *Mon. Weather Rev.*, *100*, 487–490, 1972.

Barros, A. P., and R. J. Kuligowski, Orographic effects during a severe wintertime rainstorm in the Appalachian Mountains, *Mon. Weather Rev.*, *126*, 2648–2672, 1998.

Barros, A. P., and D. Lettenmaier, Dynamic modeling of orographically induced precipitation, *Rev. Geophys.*, *32*, 265–284, 1994.

Bergeron, T., On the low-level redistribution of atmospheric water caused by orography, paper presented at International Conference on Cloud Physics, World Meteorol. Organ., Tokyo, 1965.

Bougeault, P., and P. Lacarrère, Parameterization of orographic induced turbulence in a mesobeta scale model, *Mon. Weather Rev.*, *117*, 1872–1890, 1989.

Bougeault, P., and P. Mascart, The MesoNH Atmospheric Simulation System: Scientific documentation, book 1, Météo-France, Cent. Natl. de la Rech. Sci., Paris, 2001.

Bougeault, P., P. Binder, A. Buzzi, R. Dirks, R. Houze, J. Kuettner, R. B. Smith, R. Steinacker, and H. Volkert, The MAP special observating period, *Bull. Am. Meteorol. Soc.*, *82*, 433–462, 2001.

Browning, S., Structure, mechanism and prediction of orographically enhanced rain in Britain, in *Orographic Effects in Planetary Flows*, pp. 85–114, World Meteorol. Organ., Geneva, Switzerland, 1980.

Cosma, S., E. Richard, and F. Miniscloux, The role of small-scale orographic features in the spatial distribution of precipitation, *Q. J. R. Meteorol. Soc.*, *128*, 1–18, 2002.

Cotton, W. R., and R. A. Anthes, *Storm and Cloud Dynamics*, *Int. Geophys. Ser.*, vol. 44, Academic, San Diego, Calif., 1989.

Ducroq, V., J. P. Lafore, J. L. Redelsperger, and F. Orain, Initialisation of a fine scale model for covective system prediction: A case study, *Q. J. R. Meteorol. Soc.*, *126*, 3041–3066, 2000.

Fujiyoshi, Y., B. Geng, N. Yoshimoto, S. Kanada, and T. Takeda, Structure and formation mechanism of a terrain trapped rain storm, paper presented at 12th International Conference on Clouds and Precipitation, Int. Comm. on Clouds and Precip., Zurich, Switzerland, 1996.

Gal-Chen, T., and R. C. J. Sommerville, On the use of coordinate transformation for the solution of the Navier-Stokes equations, *J. Comput. Phys.*, *17*, 209–228, 1975.

Joss, J., and A. Waldvogel, Precipitation measurement and hydrology: Radar in Meteorology, paper presented at Battan Memorial and 40th Anniversary Radar Meteorology Conference, Am. Meteorol. Soc., Boston, Mass., 1990.

Kain, J. S., and J. K. Fristch, Convective parameterization for mesoscale models: The Kain-Fristch scheme, *Meteorol. Monogr.*, *46*, 165–170, 1993.

Kessler, E., On the distribution and continuity of water substance in atmospheric circulation, *Meteorol. Monogr.*, *32*, 84 pp., 1969.

Kieffer-Weisse, A., and P. Bois, Topographic effects on statistical characteristics of heavy rainfall and mapping in the French Alps, *J. Appl. Meteorol.*, *40*, 720–740, 2001.

Kuligowski, R. J., and A. P. Barros, High-resolution short-term quantitative precipitation forecasting in mountainous region using a nested model, *J. Geophys. Res.*, *94*, 31,553–31,564, 1999.

Lafore, J. P., et al., The MesoNH Atmospheric Simulation system, part I, Adiabatic formulation and control simulations, *Ann. Geophys.*, *16*, 90–109, 1998.

Lin, Y.-L., Orographic effects on airflow and mesoscale weather systems over Taiwan, *Terr. Atmos. Ocean*, *4*, 381–420, 1993.

Miniscloux, F., J. D. Creutin, and S. Anquetin, Geostatistical analysis of orographic rainbands, *J. Appl. Meteorol.*, *40*, 1835–1854, 2001.

Morcrette, J., Description of the radiation scheme in the ECMWF model, *ECMWF Tech. Memo. 165*, 26 pp., Eur. Cent. for Medium-Range Weather Forecasts, Reading, UK, 1989.

Nakakita, E., Y. Suzuki, and S. Ikebuchi, Hierarcical Time-Scale Structure in the Dependence of Rainfall Distribution on Topography, *J. Hydrosci. Hydraul. Eng.*, *19*, 1–10, 2001.

Noilhan, J., and S. Planton, A simple parameterization of land surface processes for meteorological models, *Mon. Weather Rev.*, *117*, 536–549, 1989.

Pinty, J. P., S. Cosma, J.-M. Cohard, E. Richard, and J. P. Chaboureau, CCN sensitivity of a warm precipitation event over fine scale orography with an advanced microphysical scheme, *Atmos. Res.*, 59–60, 419–446, 2001.

Reinking, R. F., J. B. Snider, and J. L. Coen, Influences of storm-embedded orographic gravity waves on cloud liquid water and precipitation, *J. Appl. Meteorol.*, *39*, 733–759, 2000.

Sevruk, B., and S. Klemm, WMO sold precipitation measurement intercomparison : Objectives, methodology, analysis. paper presented at IAHS Symposium on Atmospheric Deposition, Int. Assoc. of Hydraul. Sci., Baltimore, Md., May 1989.

Smith, R. B., The influence of mountains on the atmosphere, *Adv. Geophys.*, *21*, 87–233, 1979.

Tateya, K., M. Nakatsugawa, and T. Yamada, Observations and simulation of rainfall in mountainous areas, in *Hydrological Application of Weather Radar*, edited by I. C. Clukie and C. G. Collier, pp. 279–295, Ellis Horwood, Chichester, UK, 1991.

Warner, T. T., E. A. Brandes, J. Sun, D. N. Yates, and C. K. Mueller, Prediction of a flash flood in complex terrain, part I, A comparison of rainfall estimates from radar, and very short range rainfall simulation from a dynamic model and an automated algorithmic system, *J. Appl. Meteorol.*, *39*, 797–814, 2000.

S. Anquetin, J.-D. Creutin, and F. Minsicloux, Laboratoire d'étude des Transferts en Hydrologie et Environnement, UMR 5564 CNRS, UJF, INPG, IRD, Observatoire des Sciences de l'Univers de Grenoble, B.P. 53 X, F-38041 Grenoble Cedex 09, France. (sandrine.anquetin@hmg.inpg.fr)

S. Cosma, Laboratoire d'Aérologie, UMR 5560 CNRS, UPS, Observatoire Midi-Pyrénées, 31400 Toulouse, France.